A new method for predicting susceptibility of austenitic stainless steels to intergranular stress corrosion cracking

S. Rahimi[1], T. J. Marrow[2]

[1]Advanced Forming Research Centre (AFRC), University of Strathclyde, 85 Inchinnan Drive, Inchinnan, Renfrewshire, PA4 9LJ

[2]Department of Materials, University of Oxford, Parks Road, Oxford, OX1 3PH

Abstract

Microstructures of type 304 austenitic stainless steel, produced through thermo-mechanical processing, were analysed with large area EBSD and optical image analysis assessments of the attacked grain boundary cluster after DL-EPR testing. The thermo-mechanically processed microstructures were exposed to acidified potassium tetrathionate ($K_2S_4O_6$) solution under tensile stress and the lengths and distributions of the initiated intergranular crack nuclei were assessed. The crack populations were quantified by fitting a Gumbel extreme value statistics distribution to evaluate their characteristic crack length. A factor (susceptibility parameter) is introduced to rank the degree of susceptibility to intergranular stress corrosion cracking of thermo-mechanically processed microstructures. This accounts for the network connectivity of the sensitised grain boundaries, the grain size and the degree of sensitisation. Similar rankings are obtained for this susceptibility parameter and characteristic crack lengths of the assessed microstructures, in which the thermo-mechanical treatments increased the population of grain boundaries with resistance to stress corrosion cracking.

Keywords: Intergranular stress corrosion cracking (IGSCC); Grain boundary character distribution; Thermo-mechanical processing; Grain boundary engineering (GBE); Sensitisation; Corrosion;

1 Introduction

Austenitic stainless steels are often used at elevated temperatures (≈ 450 °C) for critical applications due to their high temperature mechanical strengths, superior corrosion resistance, and good weldability. However, if sensitised, they become susceptible to intergranular stress corrosion cracking (IGSCC), a mode of environmentally assisted degradation, which is the progressive initiation and propagation of cracks along the network of susceptible grain boundaries when exposed to corrosive media in the presence of sufficient mechanical driving force (i.e. stress) [1-4]. Sensitisation of stainless steels generally refers to the degradation of grain boundary resistance to corrosion that may occur in service (e.g. heat affected zone after welding) or as a result of heat treatments (e.g. stress relief) [1, 3, 5, 6]. In stainless steels without sufficient stabilising elements, such as niobium, the $M_{23}C_6$ form of carbide becomes predominant which typically consists of 70-80% chromium carbide, and other elements can also substitute for chromium partially e.g. $(Cr, Fe, Mo)_{23}C_6$ [7, 8]. Intergranular carbide precipitation leads to local chromium depletion and hence a loss of corrosion resistance in the vicinity of the carbides (i.e. grain boundary) [1, 9]. These sensitised boundaries make stainless steels susceptible to intergranular corrosion (IGC) and IGSCC in corrosive environments [10]. A form of sensitisation may also occur in stainless steels exposed to irradiation by fast neutrons or protons [5, 6], and also with precipitation of grain boundary intermetallics [1, 11, 12].

The physical structure and chemistry of grain boundaries have impacts on their response to sensitisation [2, 5, 13-17]. The coincidence site lattice (CSL) model has commonly been

utilised to describe the structure of grain boundaries based on the misorientation between neighbouring grains, noted as the Σ value [18]. This notation can then be used for the classification of grain boundaries into two families of low-Σ CSL boundaries ($\Sigma \leq 29$), known as the special, and those with high-Σ values ($\Sigma > 29$), known as the random [15, 17, 18]. These two categories of boundaries have often been shown to have different properties. For instance, boundaries with low-Σ values ($\Sigma \leq 29$) are observed to have less susceptibility to chromium carbide precipitations (i.e. sensitisation) and IGSCC [2, 5, 19]. Therefore, the populations and distributions of both groups of boundaries (i.e. resistant and susceptible) affect the overall microstructure resistance to sensitisation and IGSCC. The concept of grain boundary engineering (GBE) has been proposed over the past few decades, to design microstructures with enhanced fraction of resistant grain boundaries through thermo-mechanical processing [2, 20]. These resistant grain boundaries typically include boundaries with low {hkl} index planes and low energy boundaries that are associated with the generation, growth and interactions of Σ3 annealing twins [21]. Higher fraction of Σ3 annealing twins, obtained by thermo-mechanical processing (i.e. GBE), has been observed to result in larger number of corrosion resistant boundaries, and this was shown to be associated with increased resistance to IGSCC [2, 22].

In a number of studies, several predictive approaches are proposed for the estimation of the extent of intergranular stress corrosion crack length, by classifying grain boundaries into *susceptible* and *resistant* categories based on the CSL description [23-29]. The proposed 2D models [23, 26, 27, 29] evaluate the likelihood of crack propagation and crack arrest from the information on grain boundaries with different characteristics and the connectivity between boundaries of similar properties (e.g. susceptible grain boundaries). The proposed 3D models consider the crack bridging behaviour and the interactions between the crack front with different grain boundaries, observed by synchrotron radiation, in-situ [23-25, 28, 30]. Crack bridging forms as a result of interactions between the intergranular crack with resistant grain boundaries which are not sensitised. These features have a mechanical shielding effect that improve IGSCC resistance through potential retardation of short crack propagation rates [24, 28, 31]. The binary classification of boundaries used in both 2D and 3D predictive models may not be fully representative of the boundaries' susceptibilities to IGSCC. This is due to the fact that the CSL definition of grain boundaries does not provide information about the nature of the grain boundary plane for most boundaries. The characteristics of grain boundary plane strongly affect the grain boundary structure, and classification based on Σ value (e.g. Σ3) does not account for this effect [21]. Previous studies have confirmed this by direct comparisons between networks of CSL grain boundaries obtained by EBSD with those of susceptible grain boundaries after corrosion tests [3, 32, 33].

Several qualitative [34] and quantitative [35-38] test procedures have been standardised to evaluate the degree of susceptibility of this class of steels to IGC and IGSCC. The need for a simple, quantitative and a non-destructive method of the degree of sensitisation (DOS) measurements in nickel-based alloys and stainless steels, has resulted in the development of Electro-chemical Potentio-kinetic Reactivation (EPR) testing [39]. This method of testing can be done using a single loop (SL-EPR) [38], the double loop (DL-EPR) [35, 37], or in the form of a simplified EPR method by implementing a mixture of features from both SL-EPR and DL-EPR test methods [36]. In DOS assessment using the DL-EPR method, the measured polarisation curve that applies to the matrix (i.e. activation loop) is distinguished from that pertaining to the susceptible chromium depleted grain boundaries (i.e. reactivation loop) [39]. Despite the fact that these procedures provide information on chromium depletion [1, 34] and the DOS, no account is taken of the relative susceptibility to sensitisation of grain boundaries with different characteristics. An approach has been proposed for measurement of the DOS

with the DL-EPR test, using image analysis (IA) of the clusters of attacked grain boundaries [32, 33] to characterise the DOS of the attacked grain boundaries only. In this approach, the impact of the "cluster compactness" [3] of the network of attacked grain boundaries on assessment of the DOS is addressed, by quantifying the level sensitivity of susceptible boundaries directly.

The degree of susceptibility of austenitic stainless steels to IGSCC can therefore be influenced by grain boundary character distributions (GBCD), the topology of the corrosion susceptible grain boundaries (i.e. cluster compactness) [40] and the DOS of the susceptible grain boundary networks [41, 42]. The grain size also determines the length scale of the intergranular cracking. Individually, these parameters are insufficient to predict the susceptibility of the stainless steel to IGSCC. A unified factor is required, which takes into consideration their combined influence to estimate the degree of susceptibility of thermo-mechanically treated austenitic stainless to IGSCC.

This study aims to unify these parameters in an IGSCC susceptibility factor. For this purpose, different microstructures of 304 stainless steel, produced using thermo-mechanical processing, have been subjected to standard DL-EPR assessment methods [43, 44] and also characterised using a new image analysis approach [3, 33] that is based on the geometrical properties of the attacked grain boundary network. This analysis provides the cluster compactness, which describes the connectivity of the network of the susceptible grain boundaries [3, 33]. It is used here, together with the grain size and a measure of the sensitisation of the susceptible grain boundaries to define a unified IGSCC susceptibility parameter that ranks the investigated microstructures. These microstructures were then subjected to standard IGSCC tests in acidified potassium tetrathionate ($K_2S_4O_6$), and the populations of intergranular crack nuclei were analysed using extreme value statistics (Gumbel distributions). These data are used to validate the proposed method of IGSCC susceptibility ranking of sensitised stainless steel microstructures.

2 Experimental procedures

2.1 Material

The material used in this study was cut from a plate of high carbon type 304 austenitic stainless steel having dimensions of 1 m × 1 m × 13 mm (L × W × T) and an identified rolling direction (RD). This same plate has been used in previous studies by the authors [2, 3, 32, 33, 45-48]. Table 1 shows the nominal chemical composition of the material, provided by the manufacturer. A set of blanks, with approximate dimensions of 250 mm × 32 mm × 13 mm (L × W × T) were cut from the mill annealed plate (longest direction, L, parallel to RD, with the L-W plane parallel to the plate surface). Some samples were reserved in the as received (As Rec) condition, and the remainder were solution annealed at 1050°C for 2 hours in air followed by air cooling. Some of these samples were reserved in this solution annealed (SA) condition, and the remaining blanks were reduced to a size of ~250 mm × 30 mm × 9 mm, which allowed tensile straining within the limits of the tensile testing machine (100 kN) for further thermo-mechanical processing.

Table 1: Nominal composition of type 304 austenitic stainless steel used in this study (wt.%)

Elements	***Fe***	***Cr***	***Ni***	***C***	***Mn***	***P***	***S***	***Si***	***N***
Wt. %	Bal.	18.15	8.60	0.055	1.38	0.032	0.005	0.45	0.038

The thermo-mechanical treatments, TMP1 and TMP2, comprised straining in tension to 20% and 30% engineering strain respectively along the longest specimen dimension, and then annealing for 26 hrs at 950°C. The strain was applied with an Instron standard tensile testing machine (i.e. MTS Alliance RT/100), using an extensometer with 50 mm gauge length, in air and ambient temperature at a crosshead displacement rate of 2 mm/minute. Specimens of all sample conditions, including As Rec, were then subjected to sensitisation heat treatment at 650°C for 20 hrs in ambient atmosphere. For all conditions, sufficient samples were prepared for microstructural characterisations, degree of sensitisation (DOS) assessments, and standard IGSCC experiments. For the latter, the sensitised blanks were trimmed down to 240 mm × 30 mm × 7 mm (L × W × T) dimensions. Table 2 summarises the sample conditions and the sequence of thermo-mechanical processes.

Table 2: Summary of sample conditions and thermo-mechanical processes applied for IGSCC investigations.

Microstructure	***Solution Annealing °C (hr)***	***Thermo –Mechanical Process (TMP)***		***Sensitisation °C (hr)***
		Strain (%)	***Annealing °C (hr)***	
As Received (AS Rec)	--	--	--	650 (20)
Solution Annealed (SA)	1050 (2)	--	--	
TMP 1	1050 (2)	20	950 (26)	
TMP 2		30		

2.2 Microstructure characterisations

All microstructures were characterised by electron-backscatter diffraction (EBSD). Samples with ≈10 mm × 7 mm dimensions were cut from the As Rec, SA and thermo-mechanically processed strips (TMP1 and TMP2), and ground and mechanically polished to a mirror finished condition. These were then electro-polished for about 60 secs under 45 V, using a mixture of acetic acid and perchloric acid as an electrolyte (92% + 8%), at ambient temperature with a stainless steel cathode. This was to remove ≈20 µm from the mirror finished surface (i.e. mechanically polished). For each microstructure, a large EBSD map with approximately 1.8 mm × 0.9 mm scan area, comprising of 3 × 2 arrays of individual maps with 600 µm × 450 µm scan area and 2% overlap in both directions, was collected with 1 µm step size. The EBSD maps were acquired using a fully automated HKL-EBSD system, equipped with a Nordlys II low light CCD camera, interfaced to a Philips XL-30 FEG-SEM. The EBSD data were analysed to define grain boundary character distributions using the Channel5 software by considering Brandon's criterion based on the CSL description [15, 18]. To define low angle grain boundaries (LAGB) and high angle grain boundaries (HAGB), 2° and 15° threshold angles were applied, respectively. The grain boundaries with evaluated Σ values of $\Sigma \leq 29$, including Σ1 LAGBs, were considered as boundaries with special characteristics.

2.3 Sensitisation assessment

The surfaces of the sensitised microstructures were prepared by standard grinding and polishing to a mirror finish condition and then tested using the DL-EPR method [35, 43, 44] at room temperature. An electrolyte of 0.5 M H2SO4 mixed with 0.01 M KSCN, de-aerated with nitrogen for 10 minutes, was used. A standard electrochemical cell with three electrodes, comprising of a saturated calomel electrode (SCE) and a platinum counter electrode, was

utilised. For each sample, the surface was initially exposed to approximately 300 mL of the electrolyte solution for 5 minutes with no applied current, to substantiate the open circuit potential (OCP) for the initiation of the DL-EPR tests. For the measurements of the activation current peak (Ia), the surface was then anodically polarised from the OCP to +300 mV SCE that was determined as the passivation potential, by applying a 1.67 mV/s sweep rate. For the determination of the re-activation current peak (I_r), the potential was then reversed from the passivation potential and swept back to the OCP at the same rate. At least three DL-EPR measurements, each on freshly prepared mirror finished surface, were conducted for each sample and the uncertainties are calculated as the difference between the average value and the maximum and minimum of all measurements. Following the DL-EPR testing, the chemically etched (i.e. corroded) surfaces were recorded by optical microscopy. Overlapping images covering more than 2/3 of the total surface of each sample were stitched together to create a micrograph with a total area of approximately 18 mm^2, comprising in excess of 2000 grains for the SA, microstructure and 8000 grains for the As Rec and TMP microstructures. All individual images were taken at 1798 × 1438 pixel resolution where the pixel to meter calibrations was carried out with images of the graticules obtained at the same magnification. The equivalent of one pixel in μm is 0.31 for these images.

The sensitised microstructures were evaluated by the standard DL-EPR assessment method and more recent approaches to obtain: (1) standard degree of sensitisation (DOS) which is the ratio of measured re-activation current peak (I_r) to that of anodic activation (I_a) [35, 36, 44]; (2) the standard DOS normalized by the estimated length of 2D grain boundary network, also known as the Chihal's method, denoted as the DOS_{Chihal} [44]; and (3) the standard DOS normalized by the measured length of the attacked grain boundary cluster, using an image analysis (IA) technique developed in [33], and denoted as the DOS_{IA}. The estimated length of grain boundary network used for the normalisation of the DOS by Chihal's method (i.e. DOS_{Chihal}) is obtained by using the EBSD measured grain size and a constant value of 1 μm for the width of grain boundary attack, assuming that all boundaries are equally attacked, disregarding their characteristics [44]. For the IA method, the actual attacked boundaries were assessed using the image analysis technique that also provided data on cluster compactness. The aim of this investigation was to find the relationship between the current ratio (I_r/I_a) (normalised and non-normalised) obtained by DL-EPR testing and the corresponding geometrical properties of the attacked chromium-depleted clusters obtained by image analysis. Full details on the cluster compactness measurement method are provided elsewhere [33], and it is described briefly below.

2.4 Cluster compactness measurement

The network of random grain boundaries (i.e. potentially susceptible to corrosion) were extracted from large EBSD maps, using Channel5 software, by excluding all boundaries with low-Σ CSL ($\Sigma \leq 29$) misorientation. The networks of attacked grain boundaries were also extracted from the large optical micrographs obtained after DL-EPR testing, using an in-house developed software in MATLAB. The geometrical properties of the largest clusters of connected boundaries in both assessments were measured by image processing. These two assessments of clusters of random grain boundaries and the attacked grain boundaries were considered to be characteristic of the microstructure, and their properties were implemented in a relationship to evaluate the cluster compactness (C) for different microstructures investigated in this study. This is defined using Equation 1 [3, 33].

$$C = \frac{L_M D}{A}$$

Equation 1

For each case, the cluster mass *(M)* is evaluated as the total area of the boundaries in the largest detected cluster. The cluster length (L_M) is then calculated as the cluster mass (M) divided by the average width (W_{GB}) of the chromium depleted zone, which was assessed by image analysis with a purpose-written MATLAB routine that identified and measured the line intercepts with several thousands of boundaries. This provided the mean width and standard deviation of all intercepted boundaries. To assess the clusters of random grain boundaries extracted from the EBSD maps, a constant width of 2 pixels (i.e. 2 μm) was used for the grain boundary width (i.e. W_{GB}). In Equation 1, D is the average grain size excluding twins measured from the EBSD maps, and A is the area of the smallest bounding box encompassing the largest cluster of connected boundaries [3, 33]. The dimensionless cluster compactness calculated for the largest cluster of random grain boundaries assessed from the EBSD maps is denoted as C_{EBSD}, and that calculated for the largest cluster of the chromium depleted boundaries after DL-EPR testing as C_{OIA}.

2.5 Mechanical loading and stress measurement

Previous metallographic investigation of the As Rec material found significant microstructure heterogeneity [46] that included variations in grain size and the distribution of the δ-ferrite phase. The latter is unaffected by the solution annealing treatment [46]. The specimens for IGSCC testing were manufactured by machining the sensitised sample blanks with initial thickness of 13 mm to strips with 7 mm final thickness, by removing 5 mm material from one side and then 1 mm from the other side. For all microstructures, the IGSCC experiments were carried out with the tested surface on the side from which 5 mm material was milled. This avoided differences in exposed content of δ-ferrite.

The surfaces to be IGSCC tested were electro-polished for 1 hour to remove ~200 μm from the machined surface. This was done in an electrolyte made from 92% wt acetic acid and 8% wt perchloric acid at 45 V and under controlled temperature (20 – 30 °C). A piece of type 304 stainless steel sheet with an approximate dimensions of 19 cm × 8 cm × 0.5 mm (L×W×T) was used as a cathode. A standard geometry in a form of double bend beam (DBB) specimen recommended by the ASTM standard [49] was used for the stress corrosion cracking tests. Each specimen was made by placing a 3 mm spacer between two strips, precisely in the middle, and then bending the strips over the spacer to join the ends with bolts and nuts (Figure 1). The spacer was a stack of 6 sheets with 0.5 mm thickness (i.e. 3 mm). The bolts and nuts and the spacer were all made from type 304 austenitic stainless steel to prevent potential galvanic effects. The dimensions of the spacer was selected to apply a 200 MPa nominal stress, below the elastic limit [46, 47].

Surface residual stress measurements were carried out by X-ray diffraction (XRD) using a PROTO-iXRD stress diffractometer and the $sin^2\psi$ method in accordance with NPL Good Practice [50]. An acceleration voltage of 20kV with a current of 4mA was applied to generate the X-ray using a Mn-anode Kα tube with a wavelength of λ = 0.21 nm. Measurements were made on the samples in the as machined, electro-polished and under nominal load conditions (i.e. after electropolishing, with specimens in DBB form). Average strains were obtained from eight equidistant locations, within the middle fibre with 80 mm gauge length, in two perpendicular directions of transverse (φ = 0°) and longitudinal (φ = 90°) to the length of the

strips (Figure 1a) [46]. The surface residual stresses were then evaluated from the lattice strains measured for the {311} crystallographic planes at a Bragg reflection of 156° (2θ), assuming X-ray elastic constants S1 = 1.2×10^{-6} (MPa) and ½S2 = 7.1×10^{-6} (MPa), respectively. For each point, and in both directions, the measurements were conducted at eleven ψ-offset angles in the range of maximum ± 33°; at each angle at least 10 measurements of 1 s exposure time were conducted. The uncertainties are calculated from the best fit to the plot of $sin^2\psi$ as a function of measured d spacing.

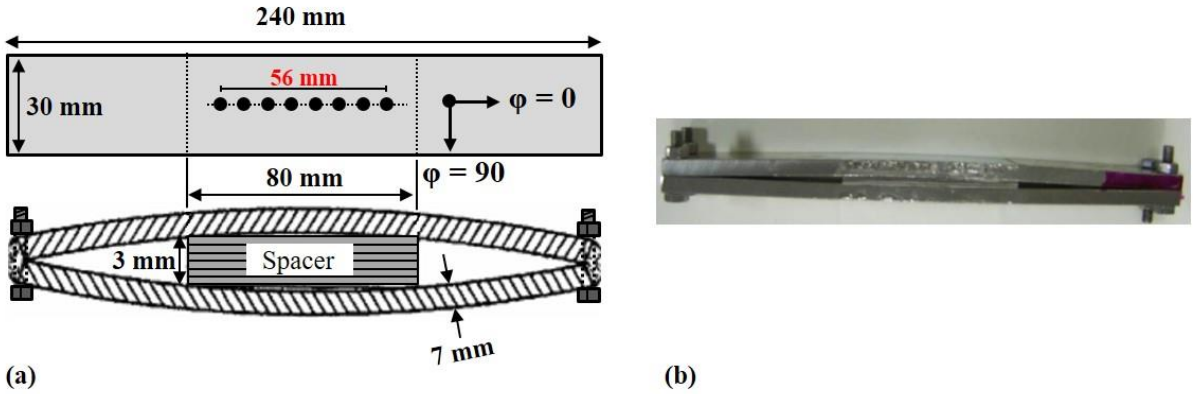

Figure 1: (a) Schematic sketches of the sample and DBB assembly used for IGSCC testing with dimensions, and the positions and directions of XRD stress measurements highlighted, (b) photograph of a DBB assembly in a loaded condition.

2.6 IGSCC tests

The loaded DBB samples were immersed together for 288 hrs in approximately 2 litres of the test solution (potassium tetrathionate, 0.1 M $K_2S_4O_6$, in deionised water). The pH was adjusted to 2.0 prior to the test by additions of dilute sulphuric acid. The DBB samples, including the spacers and the bolts and nuts were entirely coated in lacquer (Lacomit), except the area of interest (≈ 80 × 26 mm). Following the exposure time, the DBB samples were opened, cleaned with deionised water and dried. The strips (i.e. both halves) were deformed in tension to 5% of strain in an Instron mechanical test frame equipped with a 50 mm gauge length extensometer. This has been proved to be necessary to open the cracks sufficiently to make them visible for optical microscopy [46] and to reveal the crack depth when sectioned metallographically. The middle section of each strip (i.e. 80 mm gauge length) were cut out, using a band saw, and longitudinally sectioned into three pieces using a high precision diamond cutter with 0.5 mm thick blade. These 80 mm pieces were then mounted in cold resin, using standard Petri dishes as moulds, leading to four longitudinal sections per DBB, which were then prepared to a mirror finish to allow the cross-section to be investigated for crack populations using an optical microscopy. The entire length of each longitudinal piece was scanned and the longest (i.e. deepest) crack was recorded for each 2 mm interval, following the approach used in previous studies [46].

The collected data for crack lengths were evaluated using statistics of extremes [28], to provide a single representative parameter to describe the crack population. This method allows the extremes of a large crack population to be described by measuring the deepest cracks in the sample cross-section. A first type, doubly exponential, maximum value distribution that considers a normal or log normal distribution with an exponentially decreasing tail function, was used [51]. This is in a form of Equation 2 in which *Y*, the reduced parameter, can be calculated as a function of measured crack lengths.

$$Y = -\ln(-\ln(P_i))$$

Equation 2

Where $P_i = i/(n+1)$ is the empirical cumulative probability of the i^{th} data point, n is the total number of recorded cracks, and i is the location in an ascending arrangement of crack length [45-47, 52]. The cumulative probability (P_i) is the likelihood that a crack can be found among the crack population that exceeds this value. Comparisons between populations can be made at equivalent values of the reduced parameter, Y, and the characteristic IGSCC crack length was chosen at $Y = 3$, i.e. $P_i = 0.95$.

3 Results

3.1 Surface stresses

Figure 2 show the surface residual stress data for all microstructures. For all cases, the measured residual stresses are tensile in both directions (i.e. φ = 0° & 90°) in the as machined condition, in which the longitudinal stress is lower than the transverse stress. Surface machining causes heterogeneous plastic strain on the surface that leads to the generation of residual stress. This can be tensile or compressive in nature on the surface, based on the machining strategy (e.g. tool path) and the machining tool, and is typically compressive near-surface and in the substrate [46, 47, 53]. The magnitude of these stresses can be sufficiently high to drive IGSCC cracking in corrosive environment, in the absence of external load [47, 53]. Electro-polishing to remove ~200 µm material reduced the machining-induced stresses effectively. The measured stress in the longitudinal direction for the electro-polished and loaded (i.e. DBB) samples of all microstructures is close to the intended nominal applied stress of 200 MPa.

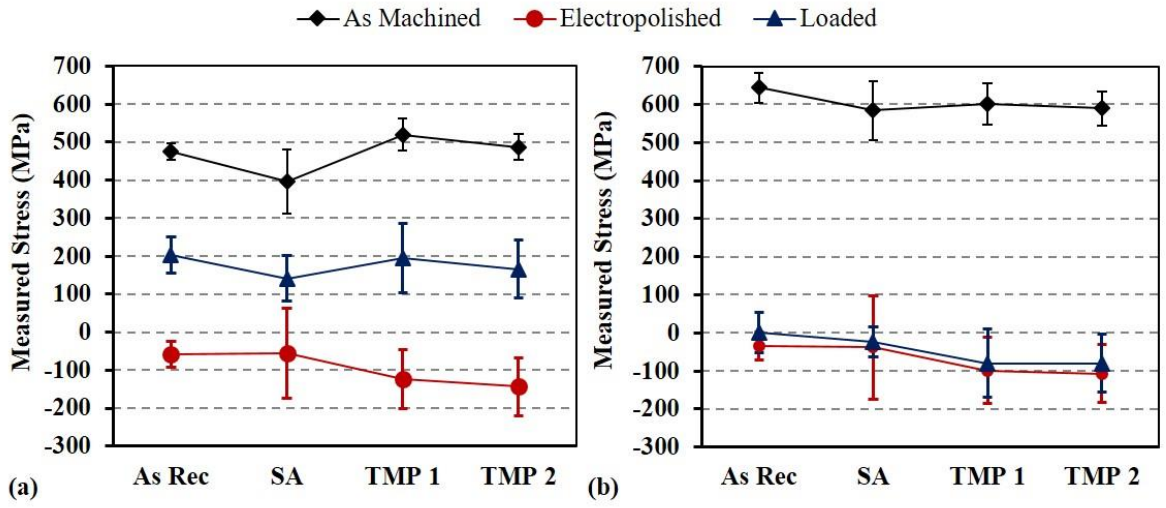

Figure 2: Measured residual stress magnitudes on all microstructures in the as machined, after 1 hour electro-polishing, and DBB loaded (i.e. 200 MPa nominal stress) conditions; (a) Longitudinal (φ = 0), and (b) Transverse (φ = 90). See Figure 1a for sample orientation.

3.2 Material and microstructure

Characteristic EBSD combined band contrast and grain boundary maps of the As Rec, SA, TMP 1 and TMP 2 microstructures (Table 2) acquired from a plane with its normal axis

perpendicular to the rolling direction (RD), are depicted in Figure 3. These show the grain size of the SA microstructure (~50 μm) is larger than the other microstructures, which have grain sizes of the order of 20 to 30 μm. Data for GBCD, triple junction distributions (TJD) and grain size, measured both including twins and excluding twins, are summarised in Table 3. The extracted data are the number and length fractions of the special grain boundaries ($1 \leq \Sigma \leq 29$), twins (Σ3), higher order twins ($\Sigma 3^n$, n = 2 and 3) and low angle grain boundaries (LAGB-Σ1). The term 'special' is assigned to boundaries with Σ value in the range of $1 \leq \Sigma \leq 29$ and is chosen for consistency with the literature. The TJD data consider the fractions of different CSL at the triple junction (n-CSL TJ, n = 1, 2, 3) and random grain boundary triple junctions (0-CSL TJ). The criterion applied to classify the triple junctions was similar to the GBCD in which boundaries with Σ in the range of $1 \leq \Sigma \leq 29$ are considered as special and those out of this range as random. For instance, a triple junction having two grain boundaries with Σ values within $1 \leq \Sigma \leq 29$ range is classified as 2-CSL TJ.

The TMP microstructures are dominated by twin (Σ3) and twin variants (Σ9, 27) (Table 3), which are the geometrically necessary features for the multiple twinning mechanism [54-58]. The number and length fractions of low-Σ CSL grain boundaries excluding twins and twin variants (i.e. $\Sigma \leq 29$ and $\Sigma \neq 3, 9, 27$) in all microstructures are mainly dominated by LAGB (Σ1) so that the proportions of other non-twin low-Σ CSL boundaries are negligible. Therefore, the total number and length fractions of the low-Σ CSL boundaries ($\Sigma \leq 29$) obtained for each microstructure are strongly influenced by the proportions of twin (Σ3), twin variants (Σ9, 27) and LAGB (Σ1) [59]. The mean populations of 1-CSL and 2-CSL TJs (Table 3) remained almost unchanged after the TMP1 and TMP2 thermo-mechanical treatments. The variance is larger for the SA microstructure, which has a coarse grain size, as there is small population of TJs. The frequency of 0-CSL TJs decreased with the increase in the populations of Σ3 and Σ9, 27 boundaries. The generation of low-Σ CSL grain boundaries, caused by twinning, decreased the proportion of 0-CSL TJs. In contrast, twinning has led to an increase in 3-CSL TJ population after the thermo-mechanical treatments.

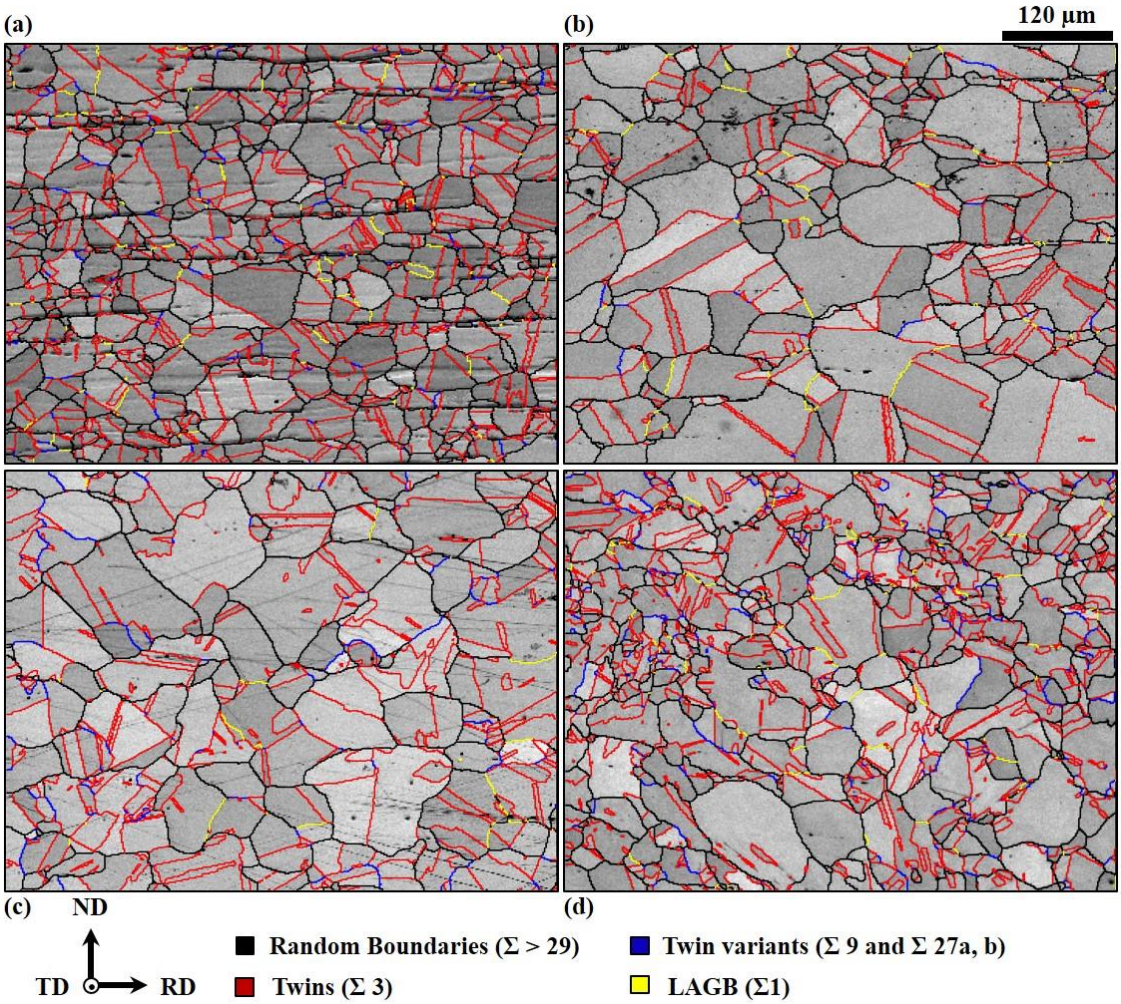

Figure 3: Characteristic EBSD orientation maps of the investigated microstructures; (a) as received, (b) solution annealed, (c) TMP 1, and (d) TMP 2. Σ3 boundary traces are shown in red, Σ9 and Σ 27a, b boundaries in blue, low-angle grain boundaries (Σ1) in yellow and random boundaries in black lines.

Table 3: Summary of data obtained from the thermally sensitised microstructures of the As-received (As Rec), solution annealed (SA) and thermomechanically processed materials (TMP1 and TMP2). Data are reported for the length and number fractions of grain boundary type (CSL, coincidence site lattice), grain size (GS), types of triple junction (i.e. number of CSL boundaries), cluster compactness obtained using EBSD and optical image analysis (C_{EBSD} and C_{OIA}), etched grain boundary width measured after DL-EPR test (W_{gb}), degree of sensitisation (DOS – see text for types of assessment) and the characteristic crack length measured in the IGSCC (intergranular stress corrosion cracking) tests.

Microstructure Characteristic		As Rec	SA	TMP 1	TMP 2
Length Fraction (%)	**Σ ≤ 29**	55.1 ± 1.8	56.1 ± 2.3	65.2 ± 1.7	62.2 ± 1.6
	Σ3	47.6 ± 1.4	49.7 ± 2.3	55.4 ± 2.5	51.8 ± 2.3
	Σ9, 27	3.3 ± 0.4	1.7 ± 0.4	6.4 ± 1.3	6.6 ± 0.5
	Σ1	2.8 ± 0.9	9.5 ± 6.0	2.9 ± 0.8	3.5 ± 1.2
	Random	44.9 ± 4.5	43.9 ± 11.0	34.8 ± 6.3	37.8 ± 6.6
GS (μm)	**+ Twins**	14.1 ± 3.7	32.7 ± 11.1	21.8 ± 5.3	14.9 ± 3.3
	- Twin	20.8 ± 0.7	49.7 ± 12.7	33.9 ± 1.2	22.8 ± 2.5
Number Fraction (%)	**Σ ≤ 29**	41.0 ± 1.4	39.5 ± 1.4	52.4 ± 1.6	49.2 ± 1.7
	Σ3	29.4 ± 0.4	29.4 ± 1.2	35.8 ± 1.6	33.1 ± 1.4
	Σ9, 27	6.0 ± 0.4	3.5 ± 0.6	11.8 ± 0.9	11.2 ± 0.2
	Σ1	2.8 ± 0.5	8.5 ± 4.6	2.6 ± 0.8	2.9 ± 0.5
	Random	59.0 ± 2.7	60.5 ± 7.8	47.6 ± 4.9	50.8 ± 3.8
0-CSL TJ		18.0 ± 1.3	19.7 ± 6.3	10.8 ± 1.5	12.8 ± 2.6
1-CSL TJ		56.2 ± 3.8	56.7 ±20.5	51.4 ± 6.4	51.6 ± 10.7
2-CSL TJ		12.8 ± 1.1	13.4 ± 3.8	14.9 ± 3.5	15.0 ± 3.2
3-CSL TJ		13.0 ± 1.5	10.2 ± 3.1	22.8 ± 2.5	20.6 ± 4.2
C_{EBSD}		1.42 ± 0.06	1.48 ± 0.26	1.02 ± 0.07	1.22 ± 0.07
C_{OIA}		1.27 ± 0.05	0.94 ± 0.06	1.11 ± 0.06	1.05 ± 0.07
$W_{gb}(\mu m)$		3.8 ± 0.4	4.3 ± 0.5	4.4 ± 0.8	4.4 ± 0.6
DOS (I_r/I_a)		0.31 ± 0.01	0.22 ± 0.01	0.27 ± 0.01	0.30 ± 0.01
DOS_{Chihal}		0.32 ± 0.10	0.68 ± 0.30	0.43 ± 0.20	0.33 ± 0.10
DOS_{IA}		0.50 ± 0.04	1.10 ± 0.07	0.59 ± 0.05	0.58 ± 0.04
Characteristic IGSCC lengths at Y = 3 *(μm)*		323 ± 50	2389 ± 72	194 ± 25	243 ± 27

3.3 Sensitisation assessment

For all microstructures, the OCP approached a steady state (i.e. stability) within 300 s with potentials typically between -0.435 to -0.450 *V* (Figure 4a). DL-EPR curves are presented in Figure 4b, with the different regions of the polarisation curves highlighted along with the activation (I_a) and reactivation (I_r) peaks for the As Rec microstructure as an example. The degree of sensitisation, DOS (I_r/I_a), calculated using the standard DL-EPR testing procedure, is summarised in Table 3 for all microstructures. The lowest DOS (~0.2) is obtained for the SA microstructure, whereas the As-Rec and TMP microstructures have DOS values that are close to 0.3. Materials with DOS above 0.05 are considered to be fully sensitised and susceptible to IGSCC [35]. Previous studies of the effect of sensitisation time on DOS in type 304 austenitic

stainless steel reported that by increasing sensitisation time, the DOS for different microstructures approaches a saturated value, with fully sensitised microstructures obtained after 20 hours exposure at 650°C [3, 33, 60].

Figure 5 shows optical micrographs of the sensitised microstructures after DL-EPR testing. Due to the smaller grain size of the As Rec material, the number of grain boundaries is higher and so the assessed length of sensitised boundaries is greater than the other microstructures. In addition to the chromium depleted boundaries, the δ-ferrite stringers have also been severely attacked. This is more apparent in the As Rec microstructure (Figure 5a). Coherent twin boundaries in all microstructures, highlighted by arrows in Figure 5, have not been strongly etched compared to the other grain boundaries.

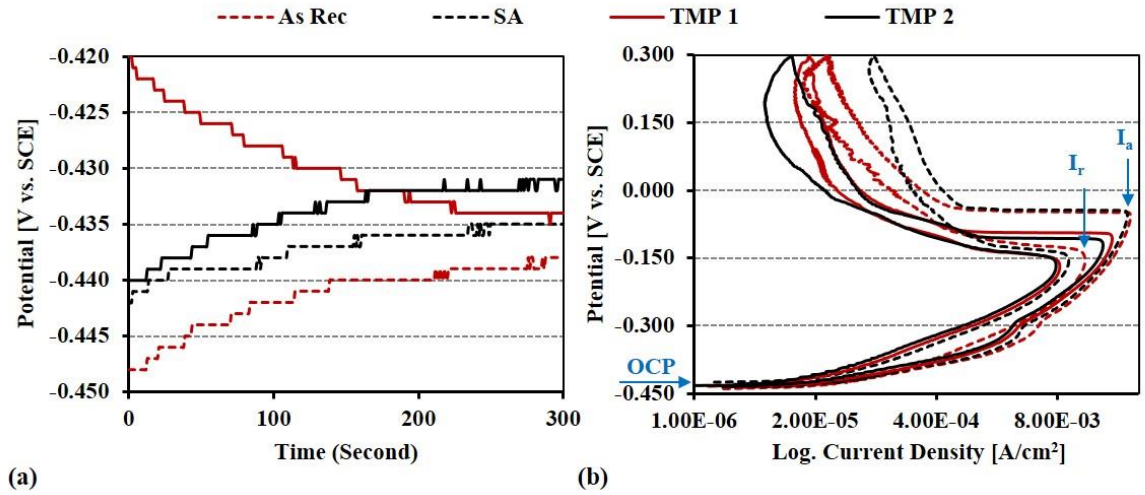

Figure 4: Plots of (a) open circle potential (OCP) as a function of time, and (b) DL-EPR traces for the investigated microstructures after sensitisation treatment at 650ºC for 20 hours. The maximum activation (I_a) and reactivation (I_r) currents are highlighted in (b) for the as received microstructure.

3.4 Cluster analysis

The largest clusters of random grain boundaries ($\Sigma > 29$), characterised using the EBSD maps, and corroded boundaries, extracted from the optical micrographs, are shown in Figure 6 and Figure 7, respectively, for all microstructures. For the purpose of visibility, these figures present only half of the total area scanned by both EBSD and optical microscopy, but the total area was used for the cluster compactness analyses (full area images are supplied as supplementary information). For the thermo-mechanically processed microstructures (TMP 1 and TMP 2), the cluster compactness C_{EBSD} [3, 33] is smaller (~1 to 1.2) than the equivalent compactness for the As Rec and SA microstructures (~1.5) (Table 3). Analysis of the distribution of corroded cluster sizes found that more than 95% of the fraction of the cluster mass belongs to one cluster in each microstructure, and that this largest cluster was fully percolative throughout the inspected area (≈ 18 mm^2). The chromium depleted cluster compactness (C_{OIA}) of the thermo-mechanically processed and SA microstructures are similar (~1) and lower than the As Rec microstructure (~1.3) (Table 3).

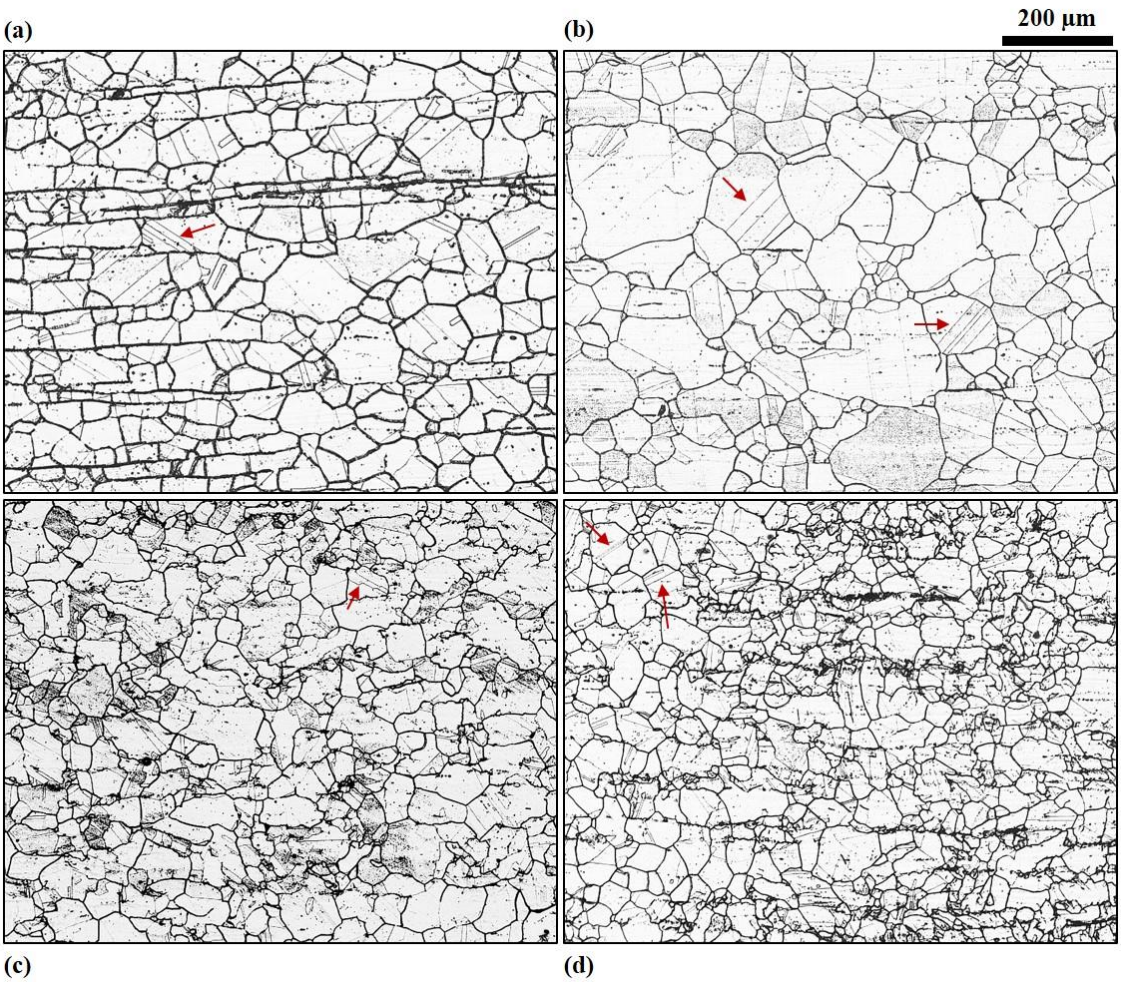

Figure 5: Optical microscopy appearance of the sensitised (i.e. 20 hours at 650ºC) microstructures after DL-EPR test, (a) As Rec, (b) SA, (c) TMP 1, and (d) TMP 2. Arrows indicate coherent twins, which are only lightly attacked during the DL-EPR test.

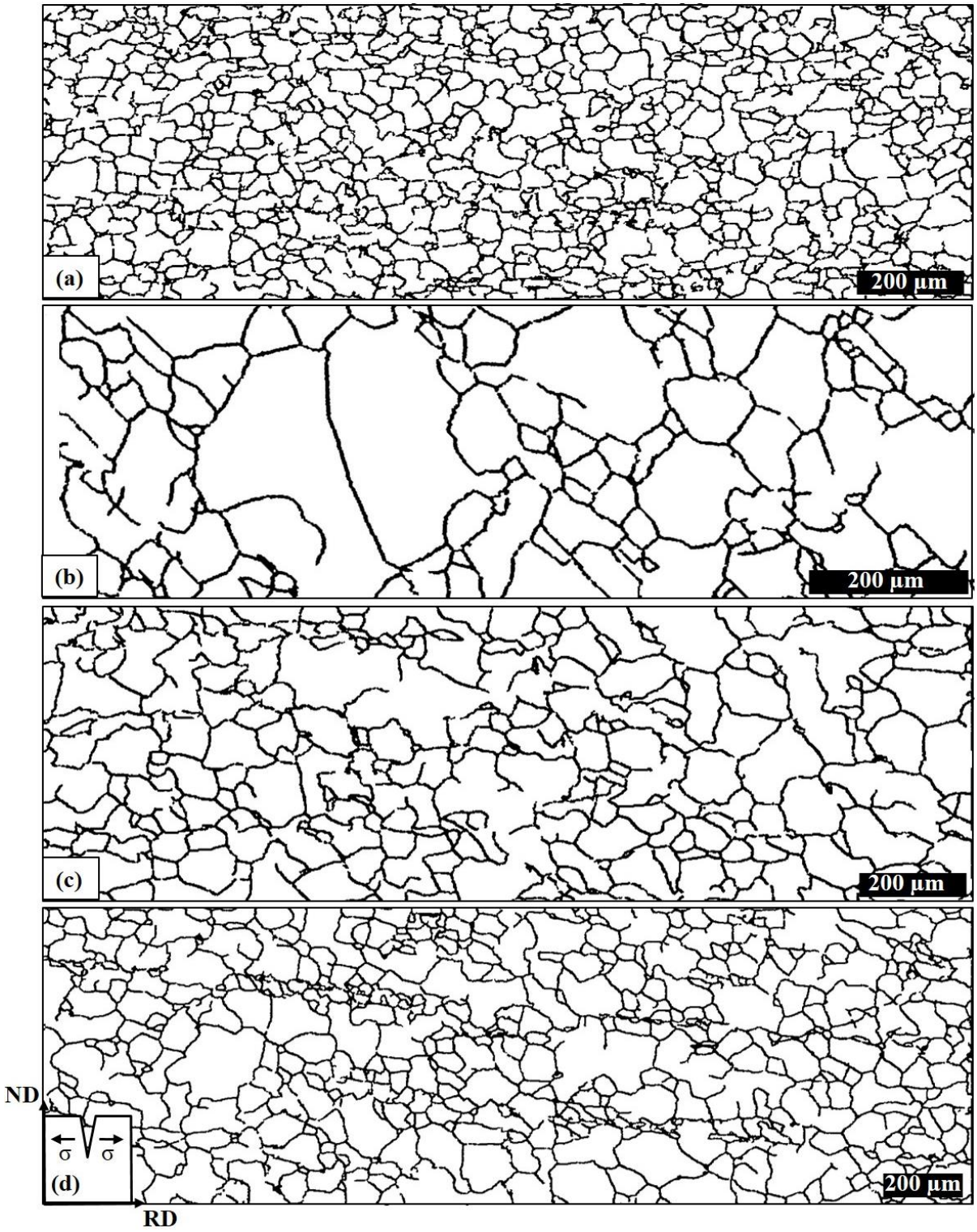

Figure 6: Largest random grain boundary (Σ > 29) cluster extracted from the EBSD map of a large area for (a) the as received, (b) solution annealed, (c) TMP 1, and (d) TMP 2. The scale bar shown on each map represents 200 µm.

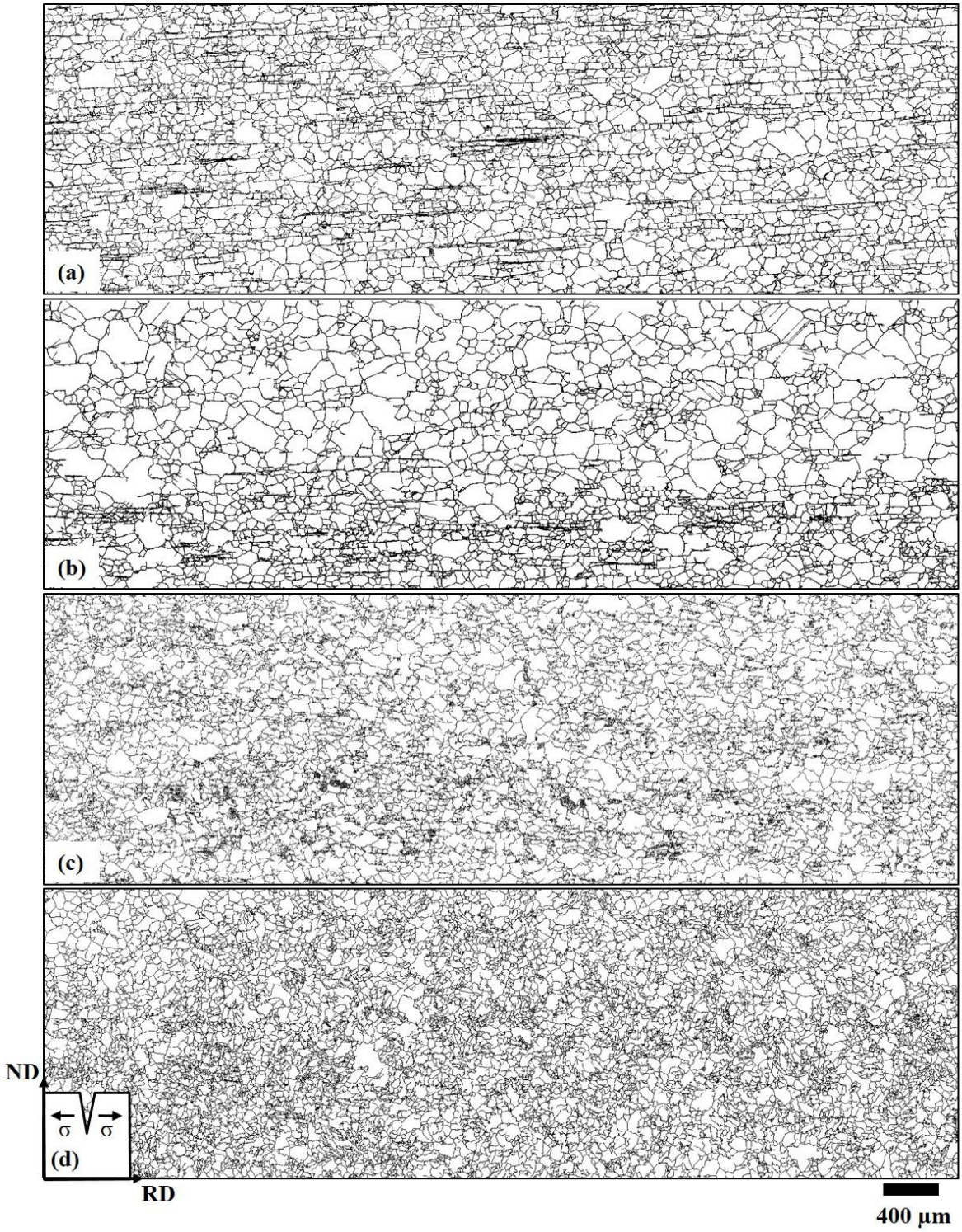

Figure 7: A largest cluster of attacked grain boundary assessed by image analysis from the large optical micrographs of the surface of fully sensitised microstructures after DL-EPR tests; (a) as received, (b) solution annealed, (c) TMP 1, and (d) TMP 2.

3.5 IGSCC characteristic crack lengths

The crack populations that developed in the four microstructures after IGSCC testing are summarised in Figure 8. All the data are presented in Figure 8a, which shows that significantly longer cracks developed in the SA microstructure; for clarity the results for only the As Rec and TMP microstructures are summarised in Figure 8b. The crack populations are compared quantitatively using the anticipated crack length in equivalent interrogation area, represented at a chosen *Y* value (i.e. the reduced parameter).

The characteristic crack lengths at Y=3 are shown in Figure 8c for all microstructures; the error bars are the 95% confidence intervals, evaluated from the co-variance of the best linear fit to the Gumbel distribution. The best fit line and the upper- and lower-bounds of the 95% confidence intervals are plotted for one of the TMP1 strips in Figure 8b. The values are summarised in Table 3. The characteristic crack length is significantly longer in the SA microstructure (~2.64 mm). The characteristic crack lengths of TMP 1 microstructure are shorter than in TMP 2 (~ 200 µm and ~ 225 µm respectively), and both TMP microstructures have shorter characteristic crack lengths than the As Rec material (~ 340 µm).

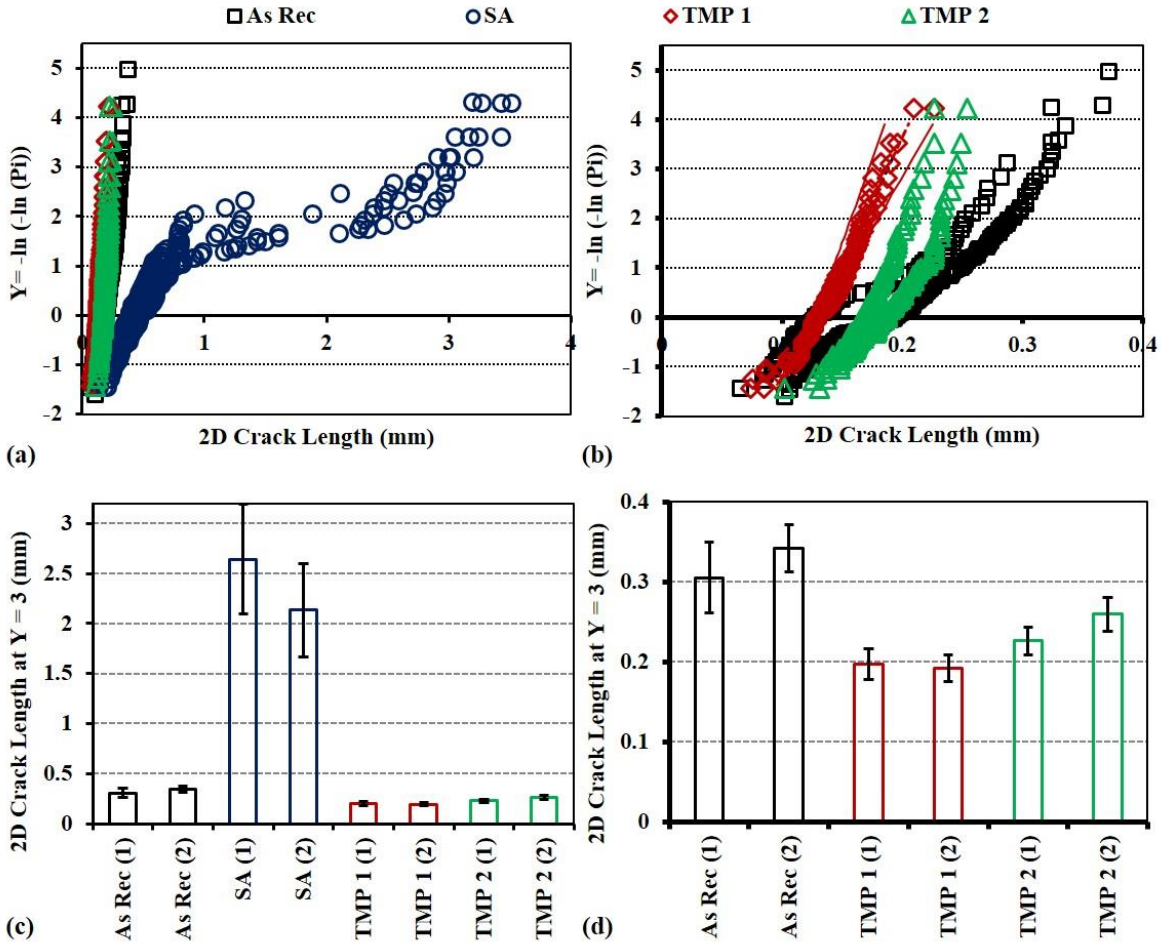

Figure 8: (a) Gumbel probability plots for the assessed cracks from different microstructures after 288 hours exposure to corrosive solution under 200 MPa nominal stress, (b) same plot as that of (a) but only for the As Rec, TMP 1 and TMP 2 to highlight the distributions of cracks for these microstructures, (c) and (d) are the expected maximum crack length from the fit to the Gumbel distribution at Y = 3 for the data in (a) and (b), respectively. Error bars in (c) and (d) are calculated from the best fit 95% confidence interval.

4 Discussion

4.1 Microstructure characteristics

Deformation and annealing treatments cause microstructural alteration through recovery, recrystallisation and grain growth [61]. The interfacial energy of high energy boundaries can be reduced through different microstructural evolutionary mechanisms such as: (i) reorientation of grain boundary plane into lower energy status [62]; (ii) formation of low energy boundaries by multiple twinning and grain boundary dissociation [63]; and (iii) reduction in grain boundary area by grain growth [64]. During thermo-mechanical treatments, a combination of all these mechanisms may take place concurrently. An appropriate thermo-mechanical treatment for improved resistance to intergranular failure, from a perspective of grain boundary design and control, would be one through which a microstructure with small grain size and maximised fraction of low-Σ grain boundaries is produced [2, 28, 45, 65, 66].

In this study, the applied single step thermo-mechanical treatments achieved microstructures with comparable grain size as that of the As Rec, but with increased fractions of low-Σ grain boundaries (Table 3). The solution annealing treatment did not cause significant changes in triple junction distribution. In the TMP microstructures the length fractions of low-Σ ($\Sigma \leq 29$) grain boundaries remained relatively unchanged; whereas their number fractions are increased compared to the SA material (Table 3). The increased frequencies of low-Σ CSL boundaries in these microstructures are due to a significant increase in the number fractions of higher order twins (Σ9, 27) compared to the SA. This is indicative of initiation of the onset of multiple twinning at 950°C as these are geometrically necessary features of the twin interactions and twin regeneration mechanisms [54, 55]. These mechanisms result in an increased number of low energy boundary segments, such as higher order twin boundaries, and also decreased grain size [63, 67, 68]. Based on the purely geometrical consideration in two dimensions, the 1-CSL TJ fraction is saturated when the frequencies of low-Σ CSL boundaries exceed the threshold of 33% [69]. In microstructures with frequencies of low-Σ CSL boundaries above this saturation threshold, more boundaries lead to the formation of 2-CSL and 3-CSL triple junctions. According to this 2D model also, the saturation threshold for 2-CSL TJ is 66%. This implies that in microstructures with low-Σ CSL frequencies above 66%, the excess boundaries are taking a part in the formation of 3-CSL TJ [69].

The increased fraction of resistant grain boundaries has resulted in disruption of the network of susceptible grain boundaries [70]. Relative to the As-Rec microstructure, the dimensionless cluster compactness, for both random grain boundary clusters (C_{EBSD}) and corroded grain boundary clusters (C_{OIA}), is decreased by thermo-mechanical processing (Table 3). This break-up of the grain boundaries cluster is a mechanism that may affect IGSCC propagation, as discontinuity in the network of susceptible grain boundaries is associated with resistant boundary segments. These segments are either twins or the boundaries associated with twins that are formed due to the interaction of twins with other interfaces [6, 14, 71-73]. The cluster compactness is a measure of network break-up that is insensitive to grain size. The calculated cluster compactness for the random grain boundary network (C_{EBSD}) showed a decreasing trend with increasing Σ3 fractions (Table 3). The compactness of the corrosion susceptible boundary network (C_{OIA}) has the same dependency on twinning (Table 3). The presence of twins in a microstructure, which is generally beneficial to stress corrosion resistance [14, 74], is therefore a marker for break-up of boundaries [75].

4.2 Crack growth behaviour

Generally, the populations of the assessed cracks can be defined by Gumbel distributions (see Figure 8a, b), implying that the bottom-line distribution can be fit by an exponentially decreasing tail function. Previous reports on IGSCC crack growth behaviour in fully sensitised type 304 austenitic stainless steel, tested in the same conditions, also showed log-normal for the parent distributions [45]. The non-Gumbel distribution of the crack lengths (Figure 8a) for the SA therefore reveals a significantly big difference in the underlying population. The largest recorded crack length may indeed be limited by the reduction in the stress level in the DBB assembly, as a result of crack opening. Nonetheless, the data obtained in this study show significantly longer cracks for the SA microstructure. Previous studies [46, 47] found that generally longer exposure time to corrosive media results in increased crack lengths, and also longer cracks were observed to be developed in microstructures with coarser grain size. These data confirm that IGSCC behaviour can strongly be influenced by microstructure in sensitised stainless steels and these can be altered by thermo-mechanical processing.

4.3 Prediction of maximum likely crack growth

The obtained GBCD and TJD data for all microstructures (Table 3) provide inputs for percolation-like crack length prediction models [26-30]. The assumption in these 2D models is that a crack will be arrested when the crack tip is confronted by a resistant triple junction. Hence, the distributions of resistant grain boundaries and triple junctions play important roles in prediction of crack length [76]. In the percolation–like models (i.e. Palumbo [27], Gertsman [29], Lehockey [26]), the probability of crack arrest, and thus the maximum likely crack length, is based on the microstructure character distributions and is also independent of the effect of external applied stress. The probabilities of arresting a crack at a given triple junction (P) and arresting a crack within the length L, for all percolation-like models, are summarised in Table 4.

Each model uses different criteria for the classification of resistant boundaries and triple junctions. In Palumbo's model, all the low-Σ ($\Sigma \leq 29$) grain boundaries are considered as resistant [27], while in Lehockey's model only the effective twins ($\Sigma 3$) and higher order twins ($\Sigma 9$ and 27) are considered as resistant boundaries [26]. Essentially Lehockey's model is a refined version of Palumbo's model, in which additional restrictions are applied in the categorisation of resistant boundaries. Also, in Lehockey's model, the twin boundaries ($\Sigma 3$) are categorised into 'neutral' and 'effective'. The neutral twins are those that are isolated in the grain interior and do not contribute in the twin-twin interaction [54, 55] during thermo-mechanical processing to produce twin variants. Hence, they do not cause any disruption in the network of random grain boundaries (i.e. no influence on the resistance to intergranular crack propagation). On contrast, the effective twins are the major cause of fragmentation of the random boundary network through the creation of twin-related segments. This includes modification to the number of triple junctions associated with the neutral twins. The Gertsman model applies the most rigorous criteria among these models by considering only twin ($\Sigma 3$) boundaries as resistant [29]. For all these percolation-like models, a crack arrest length probability of 99% has been considered ($\chi = 99\%$).

Table 4: Maximum likely intergranular crack lengths prediction models and the criteria used in each model. Note that f_{sp} is the fraction of special grain boundaries (Σ≤29), $f_{1\Sigma3}$ and $f_{2\Sigma3}$ represent the fractions of triple junctions with one and two Σ3 twin boundaries, respectively and f_0 is the fraction of grain boundaries that are unfavourably oriented to the direction of applied stress. The "*eff* '' superscript for the parameters in Lehockey's model stands for "*effective*" for which the readers are referred to Ref [26]. For the calculation of P factor for the Crack Bridging model, $f_{TJ(3\text{-}CSL)}$, $f_{TJ(2\text{-}CSL)}$ and $f_{TJ(1\text{-}CSL)}$ are the fractions of triple junctions including three, two and one special grain boundaries (Σ≤29), respectively. Also the microstructural dependent geometrical factors f_a and f_b are considered to be $f_a = 1$ and $f_b = 0.5$.

Model	Probability of crack arrest in a given triple junction (P)	probability of crack arrest within the length L	Ref
Pulombo	$P = f_{sp}^2 + 2\left[f_0 f_{sp}\left(1 - f_{sp}\right)\right]$	$(1-\chi) = (1-P)^{\frac{2L}{d}}$	[27]
Gertsman	$P = f_{2\sum 3} + f_0 . f_{1\sum 3}$		[29]
Lehockey	$P^{eff} = \left(f_{sp}^{eff}\right)^2 + 2 f_0 f_{sp}^{eff}\left(1 - f_{sp}^{eff}\right)$	$(1-\chi) = \left(1-P^{eff}\right)^{\left(\frac{2L}{d\left(\frac{3}{4}\right)^{\frac{f_{\Sigma 3}^{eff}}{0.33}}}\right)}$	[26]
Crack Bridging	$P = \frac{\left(f_a f_{TJ(2-CSL)} + f_b f_{TJ(1-CSL)}\right)}{1 - f_{TJ(3-CSL)}}$	--	[28]

In a more recent 'Crack Bridging' model [28, 30], the *P* factor (see Table 4) is evaluated by considering the 2-CSL–TJ and also those 1-CSL TJs that are unfavourably orientated to the stress axis. In this approximation, the 2-CSL triple junctions would be expected to terminate the crack, unfavourably oriented 1-CSL triple junctions only partially (50%) arrest the crack, and 0-CSL triple junctions are disregarded from having any effect on crack growth probability [30]. The Crack Bridging model considers the effect of external applied stress and crack bridging shielding effect on crack growth behaviour in which the *P* factor is used to evaluate the cumulative effect of grain bridging shielding stress on stress intensity factor at crack tip. The crack bridging shielding stress is calculated as a function of the *P* factor, ultimate tensile stress of the material (σ_{UTS}) and a saturation factor (ϕ), as shown in Equation 3 [28, 30].

$$\sigma_{br} = \phi P \sigma_{UTS}, \qquad \phi = \frac{a}{a_{sat}}$$

Equation 3

a and a_{sat} are the crack length and the saturation crack length for maximum bridging effect, respectively. A crack should propagate at least a critical distance (L_{crit}) until it encounters a bridge. This implies that for a semi-circular crack with radius a, the average crack bridging stress (σ_{br}) is zero for $a \leq L_{crit}$, and $\sigma_{br} = \frac{a - L_{Crit}}{a}$ for $a \geq L_{crit}$. The maximum shielding effect, caused by bridge formations, on stress intensity factor at the tip of the crack is then calculated through $K_{sh} = \sigma_{br}\sqrt{\left(\frac{a}{2\pi}\right)}$, so the crack opening driving force is influenced by the external applied stress and shielding stress of the bridges. Therefore the threshold stress (σ_{th}) above which a crack may propagate is expressed as a function of stress intensity factor (K_{ISCC}) at the

crack tip, and shielding stress intensity (K_{sh}) (Equation 4) [28, 30]. This simple model is only applicable for stresses in the elastic region and is not valid for stresses above the yield strength [28].

$$\sigma_{th} = \frac{\sqrt{2\pi}(K_{sh} + K_{ISCC})}{\sqrt{a}}$$

Equation 4

For the Crack Bridging model, the maximum crack lengths are estimated for a stress magnitude of 200 MPa, similar to the nominal applied stress during IGSCC tests. The crack bridging stress (σ_{br}) was calculated by assuming a saturation factor (ϕ) of 1, and σ_{UTS} of 600 MPa; this is of the same magnitude as measured for the SA microstructure in previous studies [45, 46]. The saturation crack length (a_{sat}) was determined for a maximum bridging length of 10 grains diameter using the grain size, including twins, with an assumed critical stress intensity factor (K_{IGSCC}) of 0.1 MPa$\sqrt{m}$. Since ϕ =1, then a_{sat} = a and a minimum L_{crit} of 10 grain diameters is assumed for each case. The threshold stress (σ_{th}) to propagate the saturated crack length was evaluated for all microstructures to allow their ranking.

The *P* factors for the different predictive models for all microstructures are summarised in Table 5, and are presented in Figure 9 with the predicted crack lengths as a function of grain size (including twins). Shorter crack lengths are predicted for microstructures with smaller grain size and higher *P* factor [23-25, 28, 30], so a relatively small change in grain size leads to a significant increase in the predicted crack length in the SA microstructure. The *P* factor calculated by the Lehockey and Palumbo models is significantly higher for the TMP microstructures, in comparison to the As Rec and SA, unlike the Gertsman model. This is due to the higher fractions of twin variants in these microstructures (Table 3), as the Lehockey and Palumbo models are sensitive to the fraction of these boundaries, where Gertsman model is more restrictive by considering only twin (Σ3) as resistant.

Table 5: Resistance factor (*P*) for all microstructures obtained using the predictive models summarised in Table 4.

Model	As Rec	SA	TMP1	TMP2
Pulombo	0.31	0.30	0.42	0.39
Gertsman	0.27	0.27	0.27	0.28
Lehockey	0.35	0.27	0.51	0.49
Crack Bridging	0.47	0.47	0.53	0.51

The relative susceptibilities to IGSCC that are observed in the experiments (Figure 8b) are best predicted by the Palumbo and Lehockey models. The applied single step thermo-mechanical treatments led to microstructures TMP1 and TMP2 with similar grain size as the As Rec, but with increased fractions of low-Σ CSL boundaries (Table 3). This has resulted in lower susceptibility to IGSCC of these microstructures, compared to the As Rec and the coarse grained SA. Although the *P* factor calculated by the Crack Bridging model (Table 4) is higher for the thermo-mechanically processed microstructures (Table 5 and Figure 9b), the predicted maximum likely crack growth does not match the measured characteristic crack lengths (Figure 9a). This is likely to be due to the assumptions used in the calculation of shielding stress and threshold stress, and suggests that the crack bridging model is too simplistic.

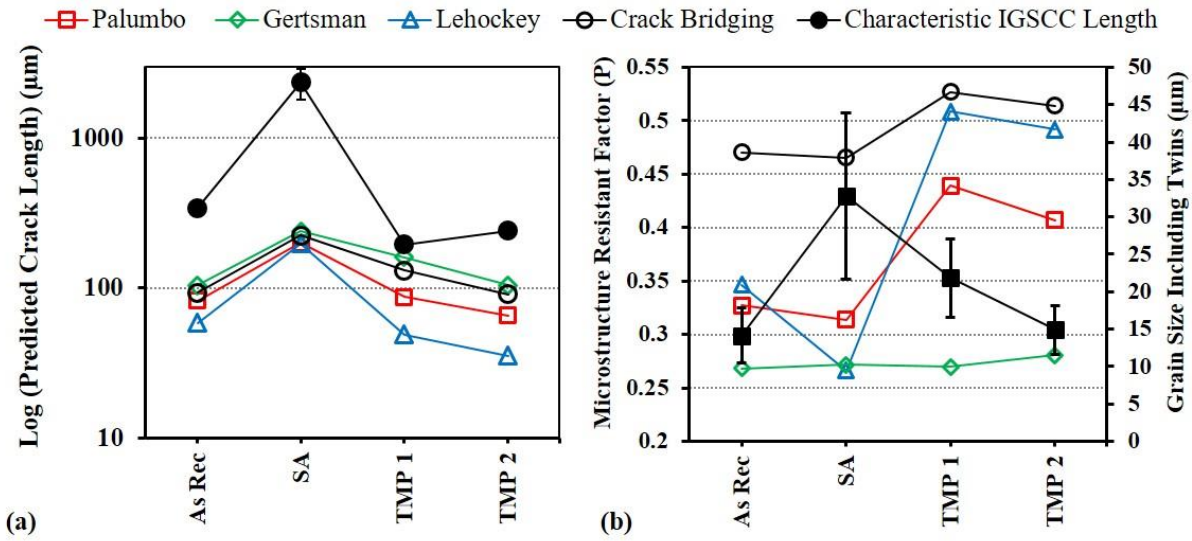

Figure 9: (a) The predicted distance of crack arrest with 99% probability by different models, and (b) the P factor and grain size including twins (Σ3) , for all investigated microstructures. The expected maximum crack length from the fit to the Gumbel distribution at Y = 3 are plotted (i.e. Characteristic IGSCC Length).

4.4 New method of ranking DOS and IGSCC

The microstructures' resistance to intergranular cracking, taking into consideration the expected crack length at Y = 3 (Figure 8), can be ranked in the following order:

$$\text{TMP1} \geq \text{TMP2} \geq As\ Rec \gg S$$

From Table 3, the evaluated C_{EBSD} and C_{OIA} data are in the following orders:

$$C_{EBSD}: \text{SA} > \text{As Rec} \gg \text{TMP2} \gg \text{TMP1}$$

$$C_{OIA}: \text{As Rec} \gg \text{TMP2} \geq TMP1 > SA$$

The trend in compactness of the clusters of corrosion susceptible boundaries (i.e. C_{OIA}) has no systematic relationship with their observed resistance to IGSCC. However, the C_{EBSD} ranking is in a good agreement with the experimental results, which indicates higher resistance to cracking with a decreased C_{EBSD} (i.e. an increase in the network break-up). The difference between the C_{EBSD} of the As Rec microstructure with that of the SA is significantly smaller than the observed difference in their resistance to IGSCC, but this can be related to the significant difference in their grain sizes.

The DOS(I_r/I_a), DOS_{Chihal} and DOS_{IA} (Table 3) are ranked in the following orders:

$$DOS\ (I_r/I_a): \text{As Rec} \geq \text{TMP2} > \text{TMP1} \gg \text{SA}$$

$$DOS_{Chihal}: \text{SA} \gg \text{TMP1} > \text{TMP2} \geq \text{As Rec}$$

$$DOS_{IA}: \text{SA} \gg \text{TMP1} \geq \text{TMP2} \geq \text{As Rec}$$

There is no systematic relationship between the DOS (I_r/I_a) and the resistance to IGSCC (Table 3). The DOS_{Chihal} does indicate higher susceptibility of SA microstructure to IGSCC, but also shows a significantly high susceptibility of TMP1 to IGSCC, which is not observed. On the other hand, the DOS_{IA} shows a higher susceptibility of the SA microstructure to IGSCC and exhibits relatively the same behaviour for the rest of the inspected microstructures. There is no systematic correlation between the IGSCC behaviour and DOS using either of the Cihal and IA approaches, but the IA ranking is closer to the ranking of IGSCC experiments. Hence, the susceptibility to IGSCC cannot be estimated by just DOS measurement, it is rather a function of materials microstructure characteristics (e.g. grain size) that have strong effects on IGSCC [3].

A method of ranking the degree of susceptibility to IGSCC of different microstructures (i.e. thermo-mechanically treated) is proposed that considers the abovementioned influential parameters. For this purpose, Equation 5 evaluates a susceptibility parameter (S_{IGSCC}), which is based on the cluster compactness (C), the DOS, which is normalised by the measured attacked grain boundary length (DOS_{IA}), and the grain size (GS). For convenience, grain size excluding twins is considered, but the grain size including twins (Σ3) would not make any difference in the calculation as these grain sizes are linearly related (Table 3). The parameter DOS_{IA} is chosen as it provides the relative degree of sensitisation of the grain boundary (essentially the average width of the attacked grain boundaries).

$$S_{IGSCC} = a\frac{(GS - \overline{GS})}{\overline{GS}} + b\frac{(C - \bar{C})}{\bar{C}} + c\frac{(\overline{DOS_{IA}} - DOS_{IA})}{\overline{DOS_{IA}}}$$

Equation 5

$\overline{GS}$, $\overline{C}$ and $\overline{DOS_{IA}}$ are the averages of grain size, compactness and DOS of the assessed microstructures, respectively. The deviations from these averages are normalised by the averages to obtain contributions to S_{IGSCC} of equal weight. Both the cluster compactness values measured for the attacked (C_{OIA}) and random (C_{EBSD}) grain boundaries clusters have been considered separately in the calculation of S_{IGCC}. The coefficients a, b and c are weighting constants, which might be adjusted in a more developed model. The evaluated susceptibility parameters for all microstructures, using both C_{OIA} and C_{EBSD}, are shown in Figure 10 assuming nominal values of $a=b=c=1$. These are compared with the characteristic IGSCC length observed in the experiments.

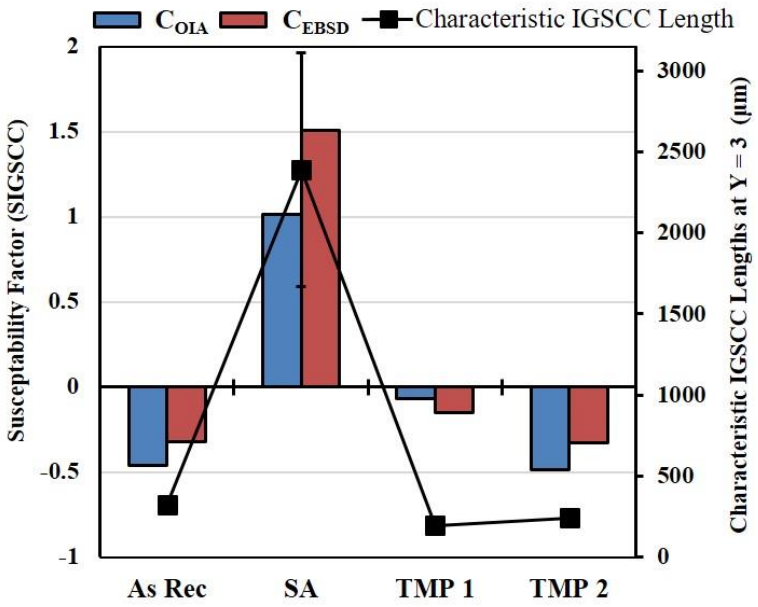

Figure 10: The susceptibility parameters (Equation 5) calculated based on nominal coefficients of 1 for all microstructures investigated in this project, based on both the cluster compactness evaluated for both the attacked (C_{OIA}) and random (C_{EBSC}) grain boundaries clusters. Characteristic crack length from the fit to the Gumbel distribution at Y = 3 are also provided for the aid of comparison.

Figure 10 shows, there is a fair relationship between the susceptibility parameter (S_{IGSCC}), calculated by considering both the attacked (C_{OIA}) and random (C_{EBSD}) grain boundaries cluster compactness values, and the measured characteristic IGSCC crack length, except for the TMP1 microstructure. This can be due to the topological connectivity of resistant and non-resistant boundaries that is not assessed by the parameters used for the calculation of S_{IGSCC}. For instance, the overall number fraction of low-Σ CSL boundaries ($\Sigma \leq 29$), particularly that of twin (Σ3) boundaries, and the fraction of 3-CSL triple junction (see Table 3) are higher for the TMP1 microstructure compared to those of the others, which is in agreement with the results of the IGSCC tests. While the distribution of number of resistant boundaries and triple junctions throughout microstructure can influence the IGSCC behaviour (i.e. crack retardation), this cannot be accounted for by the parameters used to calculate S_{IGSCC}. The S_{IGSCC} of the SA microstructure is significantly different from those of the other microstructures and agrees well with the measured characteristic crack length (Figure 10). To obtain a more representative susceptibility parameter, the weight of each parameters (i.e. the coefficients in Equation 5) need to be experimentally determined. Essentially the relative strengths of the contributions of grain size, degree of sensitisation and compactness expressed as Equation 5, can be determined with more IGSCC testing on a range of microstructures.

In the current assessment, the ranking is insensitive to the use of C_{OIA} and C_{EBSD}. However, using C_{OIA} (i.e. attacked boundaries cluster compactness) in the calculation of S_{IGSCC} (Equation 5) judged to be more relevant, as opposed to that of the random grain boundaries (CEBSD). This is because the low-Σ CSL ($\Sigma \leq 29$) boundaries are not necessarily resistant to corrosion. For instance, Figure 11 highlights the susceptibility of different types of low-Σ CSL boundaries to corrosion, after DL-EPR test. An interesting observation is the susceptibility of two curved Σ3 boundaries with misorientation angles of ≈ 55º which is significantly deviated from the 60º misorientation angle of a Σ3 twin boundary. This corroded Σ3 boundary can be coherent twin, incoherent twin or a non-twin boundary with Σ3 misorientation. Hence, the networks of

expected corrosion susceptible grain boundaries obtained by EBSD, do not necessarily represent the network of boundaries that are actually susceptible to corrosion. This might be fine-tuned in future, by determining the contributions of different grain boundaries, such as incoherent twins.

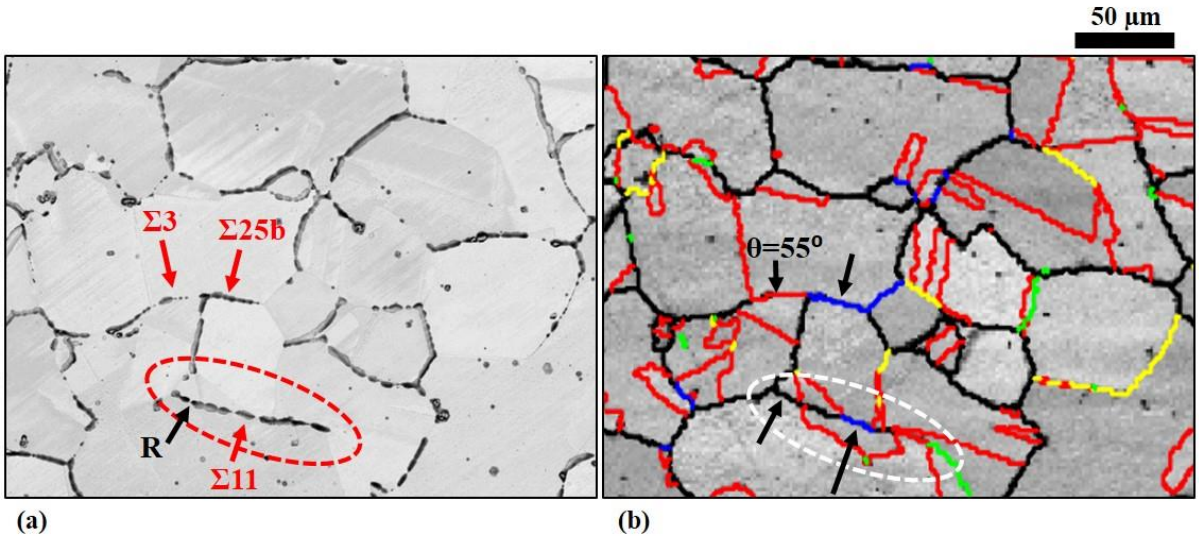

Figure 11: Microstructure appearance of the TMP1 microstructure sensitised for 20 hours at 650ºC, after DL-EPR testing, (a) SEM micrograph, and (b) characteristic EBSD map of the same area. In (b), Σ3 twin boundaries are represented in red, twin variants (i.e. Σ9 and 27 boundaries) in yellow, LAGB (Σ1) in green, the rest of low-Σ CSL boundaries (Σ ≤ 29) in blue, and random boundaries in black.

5 Conclusions

In this study, single step straining and annealing thermo-mechanical processing was used to modify grain boundary character distributions in type 304 austenitic stainless steel. The produced microstructures were subjected to detailed microstructural analyses, degree of sensitisation assessments, and intergranular stress corrosion cracking experiments. The major observations are concluded as follows:

- A new unified method is introduced to rank the susceptibility of thermo-mechanically produced microstructures of sensitised type 304 austenitic stainless steel to IGSCC that takes into consideration the modified degree of sensitisation, grain size and cluster compactness.
- Statistical evaluations (i.e. Gumbel distribution) of the populations of intergranular stress corrosion cracks in thermo-mechanically processed and sensitised type 304 stainless steel, shows a dependency of intergranular crack development on the grain boundaries character distributions.
- The cluster compactness, a purely geometrical measure of network break-up, evaluated for the random grain boundaries network (Σ > 29) obtained by EBSD, is shown to decrease with increased fraction of Σ3 twin boundaries.
- The cluster compactness measured for the network of attacked grain boundaries, following standard sensitisation test (i.e. DL-EPR testing), shows less sensitivity to microstructural changes caused by thermo-mechanical processing than expected from EBSD analyses of the same microstructures. This is shown to be due to boundaries

such as incoherent twins, which tend to be corrosion susceptible in sensitised microstructures.

6 Acknowledgements

The authors would like to acknowledge the support provided by the School of Materials at The University of Manchester during the PhD studies of S. Rahimi.

7 Data Availability

The raw/processed data required to reproduce these findings cannot be shared at this time as the data also forms part of an ongoing study.

8 References

[1] N. Parvathavarthini. Sensitisation and Testing for Intergranular Corrosion. In: H. S. Khatak, B. Raj, editor. Corrosion of Austenitic Stainless Steels Mechanism, Mitigation and Monitoring. New Delhi: Norasa Publishing House; 2002. p. 117 - 38.

[2] S. Rahimi, D. L . Engelberg, J.A. Duff, T.J. Marrow. In situ observation of intergranular crack nucleation in a grain boundary controlled austenitic stainless steel. Journal of Microscopy. 2009;233:423-31.

[3] S. Rahimi, D. L. Engelberg, T. J. Marrow. Characterisation of Grain Boundary Cluster Compactness in an Austenitic Stainless Steel. Materials Science and Technology. 2010;26:670-5.

[4] Y. J. Kwon, H. J. Seo, J. N. Kim, C. S. Lee. Effect of grain boundary engineering on hydrogen embrittlement in Fe-Mn-C TWIP steel at various strain rates. Corrosion Science. 2018;142:213-21.

[5] S. M. Bruemmer, G. S. Was. Microstructural and microchemical mechanisms controlling intergranular stress corrosion cracking in light-water-reactor systems. Journal of Nuclear Materials. 1994;216:348-63.

[6] Y. Zhou, K. T. Aust, U. Erb, G. Palumbo. Effects of Grain Boundary Structure on Carbide Precipitation in 304L Stainless Steel. Scripta Materialia. 2001;45:49-54.

[7] P. Marshal. Austenitic Stainless Steels, Microstructure and Mechanical Properties: Elsevier Applied Science; 1984.

[8] R. L. Cowan, C. S. Tedmo. In: M.G. Fontana, R. W. Staehle, editor. Advances in corrosion science and technology. New York: Plenum Press; 1973. p. 293-400.

[9] R. K. Dayal, N. Parvathavarthini, B. Raj. Influence of Metallurgical Variables on Sensitisation Kinetics in Austenitic Stainless Steels. International Material Reviews. 2005;50:129 - 55.

[10] D. G. Chakrapani. Hand Book of case history of failure analyses. In: Kholefa A. Esakul, editor. ASM International. Materials Park, Ohaio1992. p. 164 - 70.

[11] N. Sathirachinda, R. Pettersson, J. Pana. Depletion effects at phase boundaries in 2205 duplex stainless steel characterized with SKPFM and TEM/EDS. Corrosion Science. 2009;51:1850-60.

[12] N. Srinivasan, V. Kain, N. Birbilis, K. V. Mani Krishna, S. Shekhawat, I. Samajdar. Near boundary gradient zone and sensitization control in austenitic stainless steel. Corrosion Science. 2015;100:544-55.

[13] H. Kokawa, M. Shimada, Y. S. Sato. Grain-Boundary Structure and Precipitation in Sensitized Austenitic Stainless Steels. Journal of the Minerals, Metals and Materials Society. 2000;52:34-7.

[14] M. Shimada, H. Kokawa, Z. J. Wang, Y. S. Sato, I. Karibe. Optimization of grain boundary character distribution for intergranular corrosion resistant 304 stainless steel by twin induced grain boundary engineering. Acta Materialia. 2002;50:2331-41.

[15] P. Davies, V. Randle. Literature Review: Grain boundary engineering and the role of the interfacial plane. Materials Science and Technology. 2001;17:615 - 26.

[16] T. Liu, Q. Bai, X. Ru, S. Xia, X. Zhong, Y. Lu, T. Shojia. Grain boundary engineering for improving stress corrosion cracking of 304 stainless steel. Materials Science and Technology. 2019;35:477 - 87.

[17] T. Fujii, K. Tohgo, Y. Mori, Y. Shimamura. Crystallography of intergranular corrosion in sensitized austenitic stainless steel. Materials Characterization. 2018;144:219 - 26.

[18] V. Randle. The role of the coincidence site lattice in grain boundary engineering. London: Institute of Materials; 1996.

[19] H. Y. Bi, H. Kokawa, Z. J. Wang, M. Shimada, Y. S. Sato. Suppression of chromium depletion by grain boundary structural change during twin-induced grain boundary engineering of 304 stainless steel. Scripta Materialia. 2003;49:219-23.

[20] T. Watanabe. An Approach to Grain-Boundary Design for Strong and Ductile Polycrystals. Research Mechanica. 1984;11:47-84.

[21] A. King, G. Johnson, D. L. Engelberg, T. J. Marrow, W. Ludwig. Observations of Intergranular Stress Corrosion Cracking in a Grain-Mapped Polycrystal. Science. 2008;321:382 - 5.

[22] W. Kuang, G. S. Was, C. Miller, M. Kaufman, T. Alam, B. Gwalani, R. Banerjee. The effect of cold rolling on grain boundary structure and stress corrosion cracking susceptibility of twins in alloy 690 in simulated PWR primary water environment. Corrosion Science. 2018;130:126-37.

[23] A. P. Jivkov, N. P. C. Stevens, T. J. Marrow. A two dimensional mesoscale model for intergranular stress corrosion crack propagation. Acta Materialia. 2006;54:3493-501.

[24] A. P. Jivkov, N. P. C. Stevens, T. J. Marrow. A three-dimensional computational model for intergranular cracking. Compiutational Materials Science. 2006;38:442-53.

[25] A. P. Jivkov, T. J. Marrow. Rates of intergranular environment assisted cracking in three-dimensional model microstructures. Theoretical and Applied Fracture Mechanics. 2007;48:187-202.

[26] E. M. Lehockey, A. M. Brennenstuhl, I. Thompson. On the relationship betweengrain boundary connectivity, coincidence site lattice boundaries and intergranular stress corrosion cracking. Corrosion Science. 2004;46:2383-404.

[27] G. Palumbo, P. J. King, K. T. Aust, U. Erb, P. C. Lichtenberger. Grain Boundary Design and Control for Intergranular Stress-Corrosion Resistance. Scripta Metallurgica et Materialia. 1991;25:1775 - 80.

[28] T. J. Marrow, L. Babout, A. Jivkov, P. Wood, D. L. Engelberg, N. Stevens, P. J. Withers, R. C. Newman. Three dimensional observations and modelling of intergranular stress corrosion cracking in austenitic stainless steel. Journal of Nuclear Material. 2006;352:62-74.

[29] V. Y. Gertsman, M. Janecek, K. Tangri. Grain boundary ensembles in polycrystals. Acta Materilia. 1996;44:2869-82.

[30] L. Babout, T. J. Marrow, D. L. Engelberg, P. J. Withers. X-ray microtomographic observation of intergranular stress corrosion cracking in sensitised austenitic stainless steel. Materials Science and Technology. 2006;22:1068-75.

[31] A. P. Jivkov, N. P. C. Stevens, T. J. Marrow. Mesoscale mechanical model for intergranular stress corrosion cracking and implications for microstructure engineering. Journal of Pressure Vessels Technology. 2008;130:031402.

[32] S. Rahimi, D. L. Engelberg, T. J. Marrow. Characterisation of the sensitisation behaviour of thermo-mechanically processed type 304 stainless steel using DL-EPR testing and image analysis methods. 2nd INTERNATIONAL CONFERENCE CORROSION AND MATERIAL PROTECTION EFC: SVUOM Ltd; 2010.

[33] S. Rahimi, D. L. Engelberg, T. J. Marrow. A new approach for DL-EPR testing of thermo-mechanically processed austenitic stainless steel. Corrosion Science. 2011;53:4213 – 22.

[34] ASTM A262. Standard Practice for determining the susceptibility to intergranular attack in Austenitic Stainless Steels2001.

[35] A. P. Majidi, M. A. Streicher. The double loop reactivation test for detecting sensitisation in type 304 and 304L stainless steels. Corrosion. 1984;40:584 - 93.

[36] A. P. Majidi, M. A. Streicher. Four Nondestructive Electrochemical Tests for Detecting Sensitisation in Type 304 and 304L Stainless Steels. Nuclear Technology. 1986;75:356 - 69.

[37] M. Akashi, T. Kawamoto, F. Umemura. Evaluation of IGSCC susceptibility of austenitic stainless steels using electrochemical reactivation method. Corrosion Engineering. 1980;29:163.

[38] W. L. Clarke, V. M. Romero, J. C. Danko. Detection of sensitisation in stainless steels using electrochemical techniques. Houston, Texas: NACE/77, National Association of Corrosion Engineers; 1977.

[39] V. Cihal, R. Stefec. On the development of the electrochemical potentiokinetic method. Electrochimica Acta. 2001;46:3867-77.

[40] W. Huang, S. Yuan, L. Chai, L. Jiang, H. Liu, F. Wang, D. Wang, J. Wang. Development of Grain Boundary Character Distribution in Medium-Strained 316L Stainless Steel During Annealing. Metals and Materials International. 2019;25:364–71.

[41] J. Gao, J. Tan, X. Wu, S. Xia. Effect of grain boundary engineering on corrosion fatigue behavior of 316LN stainless steel in borated and lithiated high-temperature water. Corrosion Science. 2019;152:190-201.

[42] Y. Yuan, Y. Jiang, J. Zhou, G. Liu, X. Ren. Influence of grain boundary character distribution and random high angle grain boundaries networks on intergranular corrosion in high purity copper. Materials Letters. 2019;253:424 - 6.

[43] ASTM G108. Electrochemical Reactivation (EPR) for Detecting Sensitisation of AISI Type 304 and 304L Stainless Steels1999.

[44] British Standard. BS ISO 12732: Corrosion of metals and alloys - Electrochemical potentiokinetic reactivation measurement using the double loop method (based on Cihal's method)2006.

[45] S. Rahimi. Behaviour of Short Intergranular Stress Corrosion Crack in Type 304 Austenitic Stainless Steel. Manchester: The University of Manchester; 2010.

[46] S. Rahimi, T. J. Marrow. Effects of orientation, stress and exposure time on short intergranular stress corrosion crack behaviour in sensitised type 304 austenitic stainless steel. Fatigue Fract Engng Mater Struct. 2011;35:359 – 73.

[47] S. Rahimi, K. Mehrez, T. J. Marrow. Effect of surface machining on intergranular stress corrosion cracking (IGSCC) in sensitised type 304 austenitic stainless steel. Corrosion Engineering Science and Technology. 2016;51:383-91.

[48] M. Amir Siddiq, S. Rahimi. A multiscale constitutive model for intergranular stress corrosion cracking in type 304 austenitic stainless steel. J Phys: Conf Ser. 2013;451:012022.

[49] ASTM G39-99. Standard Prctice for Preparation and Use of Bent-Beam Stress-Corrosion Test Specimens2000.

[50] M. E. Fitzpatrick, A. T. Fry, P. Holdway, F. A. Kandil, J. Shackleton, L. Suominen. NPL Measurement Good Practice Guide 2005;No. 52.

[51] M. Kowaka. Introduction to life prediction of industrial plant materials: application of the extreme value statistical method for corrosion analysis. New York: Allerton Press; 1994.

[52] S. Beretta, C. Anderson, Y. Murakami. Extreme value models for the assessment of steels containing multiple types of inclusion. Acta Materialia. 2006;54:2277 - 89.

[53] K. N. Lyon, T. J. Marrow, S. B. Lyon. Influence of milling on the development of stress corrosion cracks in austenitic stainless steel. Journal of Materials Processing Technology 2015;218:32–7.

[54] V. Randle. Mechanism of twinning-induced grain boundary engineering in low stacking-fault energy materials. Acta Materialia. 1999;47:4187-96.

[55] V. Randle. Overview No. 139: Twinning-related grain boundary engineering. Acta Materialia. 2004;52:4067-81.

[56] S. K. Pradhan, P. Bhuyan, C. Kaithwas, S. Mandal. Strain-Annealing Based Grain Boundary Engineering to Evaluate its Sole Implication on Intergranular Corrosion in Extra-Low Carbon Type 304L Austenitic Stainless Steel. Metallurgical and Materials Transactions A. 2018;49:2817–31.

[57] T. Liu, S. Xia, Q. Bai, B. Zhou, L. Zhang, Y. Lu, T. Shoji. Three-dimensional study of grain boundary engineering effects on intergranular stress corrosion cracking of 316 stainless steel in high temperature water. Journal of Nuclear Materials. 2018;498:290-9.

[58] C. M. Barr, A. C. Leff, R. W. Demott, R. D. Doherty, M. L. Taheri. Unraveling the origin of twin related domains and grain boundary evolution during grain boundary engineering. Acta Materialia. 2019;144:281-91.

[59] Z. Wang, Y. Liu. Formation mechanism and application potential of Σ1 boundary in grain boundary engineering of high nitrogen austenitic stainless steel. Materials Letters. 2019;253:377-80.

[60] A. H. Advani, R. J. Romero, L. E. Murr, D. J. Matlock, W. W. Fisher, P. M. Tarin, C. M. Cedillo, J. G. Maldonado, R. L. Miller, E. A. Trillo. Deformation effects on interfacial carbide precipitation and chromium-depletion in type 304 stainless steel. Scripta Metallurgica et Materialia. 1992;27:1759-64.

[61] R. D. Doherty, D. A. Hughes, F. J. Humphreys, J. J. Jonas, D. J. Jensen, M. E. Kassner, W. E. King, T. R. McNelley, H. J. McQueen, A. D. Rollett. Current issues in recrystallisation: a review. Materials Science and Engineering A. 1997;238:219-74.

[62] Randle V. Overview No. 127 The role of the grain boundary plane in cubic polycrystals. Acta Mater. 1997;46:1459-80.

[63] R. L. Fullman, J. C. Fisher. Formation of annealing twins during grain growth. Journal of Applied Physics. 1951;22:1350-5.

[64] D. Horton, C. B. Thomson, V. Randle. Aspects of twinning and grain growth in high-purity and commercially pure nickel. Materials Science and Engineering A. 1995;203:408 - 14.

[65] Z. H. Wang, J. J. Qi, W. T. Fu. Effects of initial grain size and strain on grain boundary engineering of high-nitrogen CrMn austenitic stainless steel. International Journal of Minerals, Metallurgy, and Materials. 2018;25:922–9.

[66] A. Telang, A. S. Gill, K. Zweiacker, C. Liu, J. M. K. Wiezorek, V. K. Vasudevan. Effect of thermo-mechanical processing on sensitization and corrosion in alloy 600 studied by SEM- and TEM-Based diffraction and orientation imaging techniques. Journal of Nuclear Materials. 2018;505:276-88.

[67] C. B. Thomson, V. Randle "Fine Tuning" at $\Sigma 3^n$ boundaries in nickel. Acta Materialia. 1997;45:4909-16.

[68] M. Kumar, A. J. Schwartz, W. E. King. Microstructural evolution during grain boundary engineering of low to medium stacking fault energy fcc materials. Acta Materialia. 2002;50:2599-612.

[69] V. Y. Gertsman, J. A. Szpunar. On the grain boundary character distributions and grain boundary network topology (grain boundary statistics in materials susceptible to annealing twinning, Revisited). Scripta Materialia. 1998;38:1399-404.

[70] C. K. Kaithwas, P. Bhuyan, S. K. Pradhan, S. Mandal. Microstructure evolution during low-strain thermo-mechanical processing and its repercussion on intergranular corrosion in alloy 600H. Materials Characterization. 2018;145:582-93.

[71] E. A. Trillo, L. E. Murr. Effect of carbon content, deformation and interfacial energies on carbide precipitation and corrosion sensitisation in 304 stainless steel. Acta Materialia. 1998;47:235-45.

[72] E. M. Lehockey, G. Palumbo, P. Lin. Improving the Weldability and Service Performance of Nickel and Iron-Based Superalloys by Grain Boundary Engineering. Metallurgical and Materials Transactions A. 1998;29:3069-79.

[73] S. R. Ortner, V. Randle. A study of the relation between grain boundary type and sensitisation in a partially sensitised AISI 304 stainless steel using electron back-scattering patterns. Scripta Metallurgica et Materialia. 1989;23:1903-8.

[74] S. M. Breummer, L. A. Charlott, B. W. Arey. Sensitization development in austenitic stainless steel: correlation between stem-eds and epr measurements. Corrosion. 1988;44:328-33.

[75] S. K. Pradhan, P. Bhuyan, S. Mandal. Individual and synergistic influences of microstructural features on intergranular corrosion behavior in extra-low carbon type 304L austenitic stainless steel. Corrosion Science. 2018;139:319-32.

[76] H. Li, X. Liu, K. Zhang, W. Liu, S. Xia, B. Zhou. Effects of the triple junction types on the grain boundary carbide precipitation in a nickel-based superalloy, a statistical analysis. Philosophical Magazine. 2019;99:318-27.